

Development of Phase-Stabilized Swept-Source OCT for the Ultrasensitive Quantification of Microbubbles

R. K. Manapuram^a, V. G. R. Manne^a, and K. V. Larin^{a, b, c, *}

^a Department of Electrical and Computer Engineering, University of Houston, Houston, TX 77204, USA

^b Biomedical Engineering Program, University of Houston, Houston, TX 77204, USA

^c Saratov State University, Saratov, Russia

*e-mail: klarin@uh.edu

Received April 10, 2008; in final form, April 15, 2008

Abstract—This paper describes the development of a novel-phase resolved system based on swept-source optical-coherence tomography (SSOCT) for the ultrasensitive imaging and monitoring of gas microbubbles in aqueous media. The developed phase-stabilized SSOCT (PhS-SSOCT) system has an axial resolution of 10 μm , a phase sensitivity of 0.03 rad, an imaging depth of up to 6 mm in air, and a scanning speed of 20 kHz for a single A line. The performance of the sensing system was evaluated in water-containing gas microbubbles with a different diameter. The obtained results demonstrate that bubbles with a diameter greater than 10 μm could be detected by both structural imaging and phase response, whereas bubbles with diameters of less than 10 μm could be detected by the phase response of the SSOCT with a high sensitivity. The accuracy for the measurement of the diameter of gas microbubbles is limited to 10 μm in structural imaging and 0.01 μm in phase-sensitive monitoring. The results from this study indicate that PhS-SSOCT could be used to detect fast-moving microbubbles in aqueous solutions and ultimately could be applied for rapid assessment in biofluids (e.g., blood) and tissues (e.g., skin) in vivo.

PACS numbers: 42.62.Be

DOI: 10.1134/S1054660X08090144

1. INTRODUCTION

The development of noninvasive tools and methods for structural and functional imaging, the monitoring and quantification of biological media and tissues in vivo is extremely important for many biomedical applications including therapy, diagnostics, and the advanced imaging of various diseases. For example, the formation and/or introduction of gas microbubbles in human blood and tissues are a significant everyday clinical problem affecting thousands of patients undergoing various surgical, diagnostic, or therapeutic procedures (e.g., cardiac valve replacement, bypass surgery, and laser ablation). The formation of microbubbles in the human body has been extensively studied by many researchers since the discovery of Caisson's disease by Paul Bert in 1878. In its classic and most severe form, gas emboli present catastrophically (~4% of victims) with a collapse, a loss of consciousness, apnea, and cardiac arrest. The bubbles can travel to any part of the body, accounting for many serious (and sometimes life-threatening) disorders [1]. However, currently there is no reliable method for the prediction or diagnosis of a gas embolism prior to the commencement of apparent clinical symptoms such as severe pain in joints, pulmonary problems, etc. If the detection of microbubbles at an early stage is possible, action can be taken to prevent clinical complications.

Depending on the clinical situation, the nature of the gas emboli and the number of embolic events can vary

greatly. For example, Hills and Butler [2] measured intravascular gaseous emboli ranging from 19 to 700 μm following decompression in living dogs. Gersh detected bubble sizes between 60 and 300 μm in both intravascular and extra vascular sites. However, several studies suggested that bubbles with diameter as small as 8 μm could cause blockage and result in the trauma and onset of the symptoms [3, 4]. Therefore, in order to be effective, an imaging or sensing technique should accurately detect bubbles with diameter $\geq 8 \mu\text{m}$.

Previously, several imaging techniques have been proposed and applied to study microbubbles in blood and tissues, including Doppler sonography, magnetic resonance imaging (MRI), nuclear imaging, and computer tomography. Doppler sonography, the most popular technique since the air–bubble interface produces a strong ultrasonic reflection in the region of 1 to 20 MHz, is an ultrasound diagnostic imaging technique, enhanced with a Doppler effect, capable of assessing moving bubbles by calculating the frequency shift of a particular sample volume [5, 6]. However, Doppler sonography can detect only moving intravascular bubbles with a diameter of approximately 50 μm [2, 7, 8]. Evidently, the resolution of this imaging method should be improved in order to achieve sensitive imaging and to assess small μm -sized bubbles. Also, a new method has to be developed for the detection of stationary bubbles in tissue that could be used for the prediction or diagnosis of gas emboli.

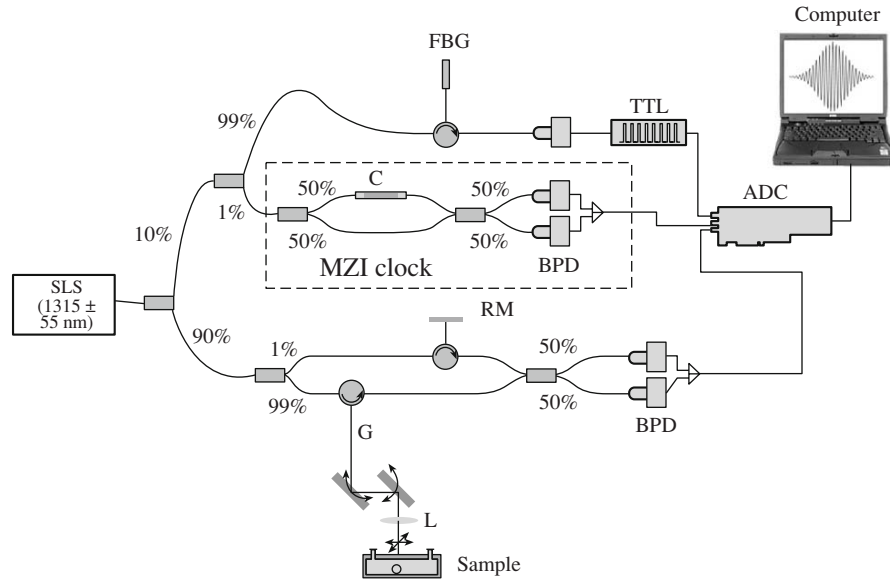


Fig. 1. The schematic outline of the phase-stabilized SSOCT system (ADC, analog-to-digital converter; BPD, balanced photodetector; C, collimators; FBG, fiber-Bragg grating; G, galvanometer scanner; L, lens; RM, reflective mirrors; SLS, swept-laser source; TTL, TTL signal generator).

Optical interferometric techniques are extremely sensitive to local changes in the scattering, absorption, and refractive index of the tissues and cells [9–13]. Since the average refractive indexes of blood, skin, and air are quite different (1.4, 1.55, and 1.0, respectively, in the near-infrared spectral range), an optical-based sensor will be capable of assessing the formation of gas bubbles with an ultrahigh sensitivity and accuracy. Optical coherence tomography (OCT) is a low-coherence interferometric technique that provides depth-resolved images of tissues with a resolution of up to a few micrometers at depths of up to several millimeters [14]. OCT has been studied for a wide range of biomedical and nonbiomedical applications [15–17], including the noninvasive monitoring of the blood glucose concentration [18–20], measuring the microflows in the scaffold structures [21] and dermatology [22].

In OCT, a two-beam interferometer is used to detect the backscattered photons from a tissue of interest within the coherence length of the laser source. Typically, a broadband low-coherence laser source is split into two arms (the reference and sample arms). The scattered light from the sample is captured in such a way that it recombines with the light from the reference arm, which results in the formation of fringes, provided the distance traveled by light in both arms does not differ by more than the coherence length of the laser source. The interference signals are recorded by the photodetector which is given by Eq. (1):

$$i(t) \propto 2\sqrt{P_r P_s} \cos 2k\delta(t), \quad (1)$$

where $i(t)$ is the recorded signal from the detector and $\delta(t)$ is the introduced path difference. P_r and P_s are the

optical powers from the reflected and the sample arms, respectively, and k is the wave number. The equation shows only the signal in the interferometric term neglecting the zero frequency component. Rewriting Eq. (1) will yield

$$i(t) \propto \text{Real} \left\{ \int S(\omega - \omega_0) e^{-j\Delta\phi(\omega - \omega_0)} \frac{d(\omega - \omega_0)}{2\pi} \right\}, \quad (2)$$

where $\Delta\phi(\omega) = \frac{2\pi}{\lambda} \Delta\delta(\omega)$ is the phase delay due to the path difference $\delta(\omega)$, and $S(\omega)$ is the spectrum of the source. The $i(t)$ and $\Delta\phi(\omega)$ are Fourier transform pairs; thus, by applying a complex fast Fourier transform (FFT) algorithm to $i(k)$, which is $i(t)$ in the k space ($k = 2\pi/\lambda$), one can obtain a 1D OCT depth profile. By generating a transversal set of a similar 1-D depth profile with a scanning galvo-mounted mirror, a 2D image could be constructed. Thus, a 2D image contains both axial and transverse information.

In this paper, we present the results of the development of a novel phase-resolved sensing system based on a swept-source optical-coherence tomography and evaluate its performance by quantifying microbubbles of different diameters in clear media.

2. MATERIALS AND METHODS

2.1. Experimental Setup

A schematic diagram of the developed PhS-SSOCT system is shown in Fig. 1. The system consists of four main units: the source, the interferometer (Mach-Zehnder in this particular setup), the calibration sys-

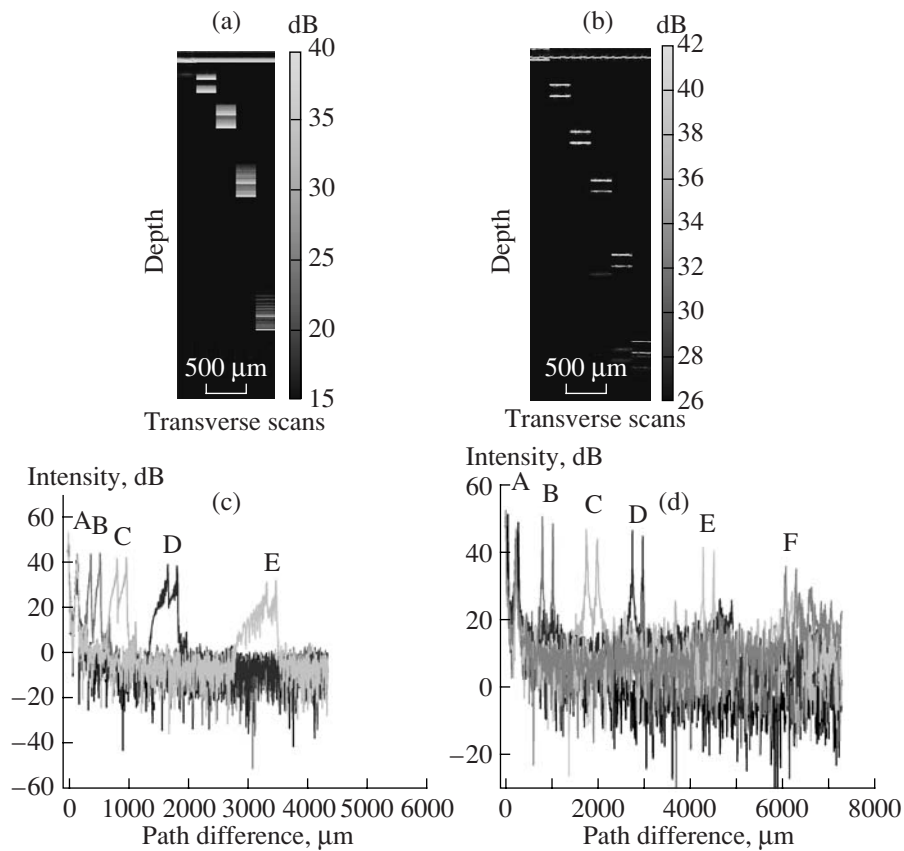


Fig. 2. 2D images of a glass slide of thickness 0.16 mm at different depths before (a) and after (b) recalibration and remapping to equal the k space and (c, d) corresponding 1D depth profiles. A, B, C, D, E, and F are the A-line scans at different depths.

tem, and the data acquisition electronics. The source is a broadband swept-source laser (Santec, Inc.) with peak output power $P = 13$ mW at central wavelength $\lambda_0 = 1315$ nm, coherence length $l_c = 13$ mm, and spectral width $\Delta\lambda = 110$ nm. One scan over the full operating wavelength range is acquired in approximately 50 μ s (corresponding to a scanning rate of 20 kHz). The light from the swept-source laser is delivered to the interferometer, where it splits into the reference and the sample arm. Light returned from the sample and reference arms form an interferogram, which is detected by a balanced photodetector (Thorlabs, Inc.). The employment of the balanced photodetector reduces the source intensity noise as well as the autocorrelation noise from the sample. The signal from the detector is digitized using a 14-bit analog-to-digital converter (ADC) (National Instruments, Inc.) and recorded by a PC.

As noted earlier, applying a complex FFT algorithm to the time-domain fringe data will yield the depth profile (A scan). However, the Fourier transform relationship requires linear tuning sweeps in the k space. The nonlinearity in the tuning curve results in the degradation of the resolution in the z space as shown in Fig. 2. The time-domain fringe data has to be recalibrated and remapped into the linear k space. Here, it is implemented using a Mach-Zehnder interferometer (MZI)-

based optical clock (MZI-OC) that generates an equally spaced frequency interferogram. All peaks as well as the zero crossings in the recorded fringes are equally spaced in the optical frequency space and, thus, the fringe data corresponding to these peaks and zero crossings are linearly distributed in the k space [23]. For the phase-sensitive measurements, the MZI-OC interferogram is recorded only once using a separate ADC channel in order to minimize the random-phase noise introduced by the MZI-OC between successive A-line scans. The fringe data from the sample corresponding to the zeros and peaks of the MZI-OC interferogram are recorded and interpolated to get a standard number (typically 2048) of data points that allow us to achieve the maximum attainable imaging depth of 6 mm in air as shown in Fig. 2d. Since the backscattered light at a depth greater than the coherence length of the laser source cannot form fringes, the maximum imaging depth would not exceed the coherence length of the laser source. In addition to that, the full-depth image is divided into two halves due to the symmetry of the Fourier transform: the first half showing the mirror image of the other half. In this system, the mirror image was ignored resulting in an imaging depth of half the coherence length, i.e., roughly 6 mm. In this setup, the free space in the delay arm of the MZI-OC was kept at a dis-

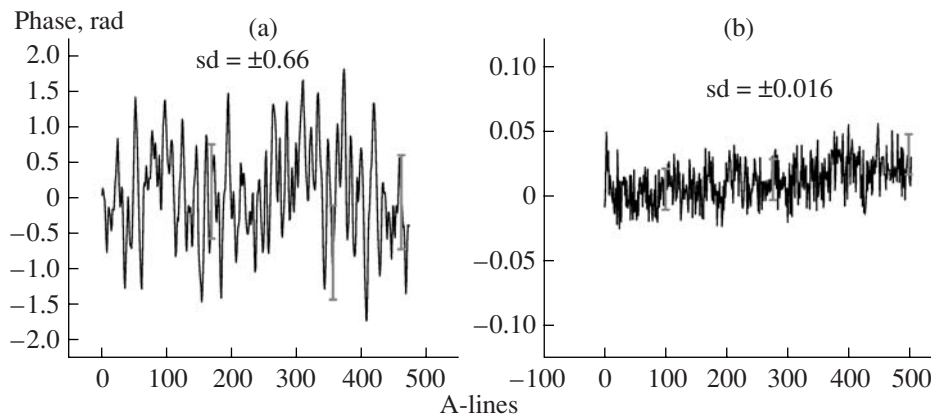


Fig. 3. Temporal-phase response of SSOCT (a) before and (b) after stabilization (note the scale difference).

tance that produces 600 peaks, thus giving 600 sample points. Here, 88 sample points were removed from the two ends of the MZI-OC. Now, to get 2048 data points, three points are inserted by spline interpolation between the remaining 512 points (inserting a lower number of points, e.g., two, might result in losing some of the higher frequency components, which, in turn, might reduce the imaging depth of the system).

The developed system was initially characterized by using a cover-glass slide (0.16-mm thick) placed in the sample arm of the interferometer. A cover-glass slide is placed at five different distances from the reference arm and imaged without and with the MZI-OC calibration (shown in Figs. 2a and 2c, respectively). Figures 2b and 2d show the corresponding 1D depth profiles. These data clearly demonstrate that the resolution is degraded without proper calibration and remapping into the k space. Figures 2c and 2d show that after proper recalibration and remapping into the k space, there was no degradation in the resolution and the maximum imaging depth of 6 mm is achieved.

In general, the path difference corresponding to the 3-dB drop in the 1D profile yields the axial resolution of the system. For the developed PhS-SSOCT, an axial resolution of 10 μm and a transverse resolution of 28 μm at a 20-kHz speed of an A-line scan were obtained. The theoretical axial resolution is 7 μm (computed as $\Delta z = \frac{2(\ln 2)\lambda^2}{\pi\Delta\lambda}$). The mismatch in the theoret-

ical and measured values is attributed mainly to the dispersion effects: the utilized imaging lens (KBX025, Newport Corporation) disperses the ends of the wavelength scans making those wavelengths partially incoherent, which effectively reduces the wavelength range and, thus, increases Δz . The transverse resolution can be enhanced by using a high-numerical aperture lens compromising the imaging depth. However, Y. Verma et al. recently have shown that the use of a tapered single-mode fiber could increase the transverse resolution

without a significant decrease in the imaging depth [24].

Although the wavelength scan is very consistent from scan to scan in the employed swept-source laser, there is a jitter on the output trigger due to the noise in the electronics and a slow drift over time. These drifts introduce varying delays between the trigger signal and the subsequent digital fringe data resulting in phase jumps of up to a maximum value of π as shown in Fig. 3a. These jumps could be removed by triggering the ADC using an electrically tunable TTL signal generated from a narrow band (0.1 nm) fiber-Bragg grating (FBG) as shown in Fig. 1 [25]. A reflected optical pulse is generated whenever the source sweeps the FBG reflection wavelength. This pulse is converted into a TTL signal using a signal generator (Stanford Research Systems). By triggering the ADC with the above TTL signal, the jitter due to the electronics is reduced by introducing a perfect synchronization between the source and data acquisition, which, in turn, reduces the phase variations; a standard deviation of 0.016 rad for 512 A-line scans has been achieved as shown in Fig. 3b.

2.2. Samples and Methods

The performance of the developed system was evaluated in water containing gas microbubbles with different diameters. Water is injected into a 500- μm flow-through cuvette (Type 48, NSG Precision Cells, Inc.) and bubbles were generated by introducing different pressures using a peristaltic pump (Fisher Scientific).

The amplitude of the interference signals in the time-delay domain was recorded from the cuvette. Four characteristic interferometric peaks were observed corresponding to the interferences between the four surfaces of the cuvette. In these experiments, the optical delay was calculated as a function of the dynamic refractive index (modified by the presence/absence of microbubbles) from the interferometric peaks in the time-delay domain produced by the reflection from the inner walls of the cuvette. The phase is monitored at the

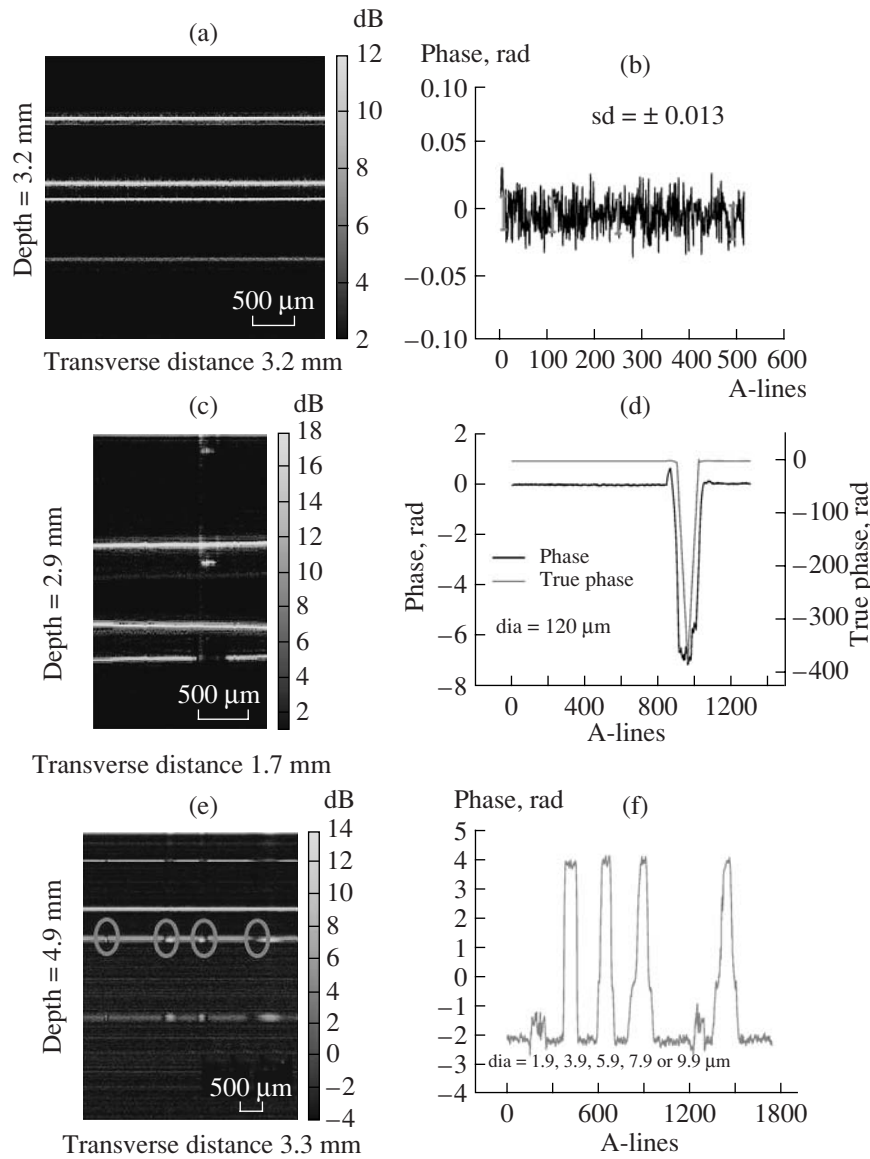


Fig. 4. 2D image of the cuvette with water: (a) with no bubble, (c) with a large bubble, (e) with bubbles with a diameter of less than $10\ \mu\text{m}$, and (b), (d), (f) corresponding temporal-phase responses.

interferometric peak that corresponds to the self-interference between the inner-glass surfaces. The self-interference is usually observed whenever the sample arm itself contains a partially reflective surface that acts as a reference arm. The phase was measured from the complex FFT and unwrapped to remove any $\pm 2\pi$ jumps. Phase-sensitive measurements of water are taken before and after injection of the microbubbles. Since the bubbles induced changes in the refractive index, the diameter of the bubble from the phase shift was calculated as

$$\frac{dn}{dC} = \frac{1}{l} \frac{\lambda}{4\pi dC} \frac{d\phi}{dC} \quad (3)$$

where dn is the refractive index change introduced by the bubble (equal to 0.33), l is the diameter of the bubble, and $d\phi$ is the bubble-induced phase shift.

3. RESULTS AND DISCUSSIONS

Figure 4a shows an image of a $500\text{-}\mu\text{m}$ cuvette filled with water. The corresponding temporal-phase response is shown in Fig. 4b. The reference arm is placed at such a distance that the top part of the image contains an area of the cuvette where bubbles are expected. Therefore, the first two bright lines correspond to the inner surfaces of the cuvette and the next two lines are the negative image of the top surface (originating due to symmetry of FFT) and the cuvette's

bottom surface, respectively. In clear aqueous media, the maximal phase variations were as low as 0.03 rad after five-point averaging, which implies that any microbubble that introduces a random phase greater than 0.03 rad can be easily detected. Images of the clear media containing a bubble of diameter 120 μm and its corresponding phase responses are shown in Figs. 4c and 4d, respectively. Note that the self-interference image of the bubble is also seen in Fig. 4c.

Generally, for an optical path difference of one wavelength, the phase shift would be 2π in a homogeneous media. Equation (3) describes the relationship between changes in the refractive index and the phase of the SSOCT system. For an air bubble in water, the change in the refractive index would be 0.33, which translates into a minimum bubble size of 2 μm for the phase to be unwrapped by one 2π jump. Since the system's resolution is 10 μm , bubbles with diameters greater than 10 μm can be clearly seen in the structural image, as shown in Fig. 4c. When there is no bubble, the optical path length between the inner surfaces of the cuvette is 665 μm (refractive index of water is 1.33, so $500 \times 1.33 = 665 \mu\text{m}$), which is observed as a peak at 665 μm corresponding to a 1D depth profile (not shown). As the beam interacts with the bubble, the optical path length keeps decreasing until it reaches the center of the bubble and increases again to the original value. This change in the optical path length is reflected as a shift in the peak in the corresponding 1D profile. The larger the bubble, the greater the decrease in the optical path length and, hence, the greater the shift. The number of 2π jumps by which the phase is unwrapped is then calculated from the peak shifted in the 1D profile. This unwrapped phase is then added to the PhS-SSOCT phase response to get the true phase response.

For the bubble shown in Fig. 4c, the true value of the phase was calculated to be 377.6 rad (by adding 59 of 2π jumps the initially measured PhS-SSOCT phase of 7.1 rad as described above). The size of the bubble was calculated as 119.8 μm by substituting the calculated true phase in Eq. (3). Similarly, several bubbles with different diameters (52, 94, 160 μm , etc.) were taken and quantified. The obtained error ranged from 0.19 to 10 μm , which can be attributed to the 2π ambiguity. A change in the path differences of less than 10 μm is not reflected in the 1D profile (due to the limited imaging resolution of 10 μm). In this case, the number of 2π jumps by which the phase should be unwrapped cannot be determined and can take any integer value between 1 and 5. This means that microbubbles with diameters that are multiples of 2 μm (up to 10 μm) would show the same phase response. For instance, if the number of 2π jumps calculated from the phase shift is 60, the actual number of 2π jumps can be any number between 60 and 65. Likewise, if the measured diameter of a bubble is 120 μm , then the actual bubble diameter could be 120, 122, 124, 126, or 128 μm . However, this ambiguity can be resolved by implementing a fast real-time continuous unwrapping algorithm, which will be devel-

oped in our future studies. This algorithm would acquire multiple-phase recordings between consecutive changes in the path difference of 2 μm and the continuous unwrapping of the phase information.

Figure 3b shows an example of small bubbles which cannot be resolved from SSOCT structural imaging. These bubbles can, however, be detected by the PhS-SSOCT. The sizes of the bubbles were estimated to be 1.9 μm (but could be 3.9, 5.9, 7.9, or 9.9 μm due to the ambiguity discussed above). The phase response also depicts a small disturbance, which can be postulated as another bubble with a size of less than 1 μm . Therefore, PhS-SSOCT is an effective device for the ultrasensitive quantification of microbubbles with diameters significantly less than the imaging capabilities of the employed system.

4. CONCLUSIONS

In this paper, we demonstrated that the PhS-SSOCT is capable of imaging, detecting, and quantifying large and small microbubbles in clear media. The results suggest that small microbubbles with a diameter beyond the imaging capabilities of the system can be detected and quantified using the PhS-SSOCT. Potentially, microbubbles with diameters as small as 0.01 μm (that introduce a phase shift of 0.03 rad) can be detected and quantified with this method. Our future studies will focus on the development of the effective phase-unwrapping algorithm that will quantify the microbubbles in both clear and blood simulated media as well as in tissues in vivo with no 2π ambiguities.

ACKNOWLEDGMENTS

The study is supported by a grant from the Office of Naval Research. The authors would like to thank Narendran Sudheendran and Esteban F. Carbajal for extensive discussions and the analysis of the results presented in this paper.

REFERENCES

1. T. S. Neuman, *News Physiol. Sci.* **17**, 77 (2002).
2. B. A. Hills and B. D. Butler, *Undersea Biomed. Res.* **8**, 163 (1981).
3. R. S. Meltzer, P. W. Serruys, J. McGhie, et al., *British Heart J.* **44**, 390 (1980).
4. A. Bouakaz and N. de Jong, *Ultrasound Med. Biol.* **33**, 187 (2007).
5. R. Y. Nishi, in *The Physiology and Medicine of Diving*, Ed. by P. B. Bennett and D. Elliott (Saunders, London, 1993).
6. D. N. Walder, A. Evans, and H. V. Hempleman, *Lancet* **1**, 897 (1968).
7. R. G. Eckenhoff, C. S. Olstad, and G. Carrod, *J. Appl. Physiol.* **69**, 914 (1990).
8. M. Malconian, P. B. Rock, J. Devine, et al., *Aviat Space Environ. Med.* **58**, 679 (1987).

9. K. V. Larin, T. Akkin, R. O. Esenaliev, et al., *Appl. Opt.* **43**, 3408 (2004).
10. I. V. Larina, E. F. Carbajal, V. V. Tuchin, et al., *Laser Phys. Lett.* **5**, 476 (2008).
11. V. V. Tuchin, *Optical Clearing of Tissues and Blood* (SPIE Press, Bellingham, WA, 2005).
12. M. Ghosn, V. V. Tuchin, and K. V. Larin, *Invest. Ophthalmol. Visual Sci.* **48**, 2726 (2007).
13. M. G. Ghosn, E. F. Carbajal, N. Befrui, et al., *J. Biomed. Opt.* **13**, 010505(3) (2008).
14. D. Huang, E. A. Swanson, C. P. Lin, et al., *Science* **254**, 1178 (1991).
15. A. M. Zysk, F. T. Nguyen, A. L. Oldenburg, et al., *J. Biomed. Opt.* **12**, 051403 (2007).
16. D. Stifter, *Appl. Phys. B: Lasers Opt.* **88**, 337 (2007).
17. B. E. Bouma and G. J. Tearney, *Handbook of Optical Coherence Tomography* (Marcel Dekker, New York, 2002).
18. K. V. Larin, M. Motamedi, T. V. Ashitkov, and R. O. Esenaliev, *Phys. Med. Biol.* **48**, 1371 (2003).
19. K. V. Larin, M. S. Eledrisi, M. Motamedi, and R. O. Esenaliev, *Diabetes Care* **25**, 2263 (2002).
20. K. V. Larin, M. G. Ghosn, S. N. Ivers, et al., *Laser Phys. Lett.* **4**, 312 (2007).
21. B. Veksler, E. Kobzev, M. Bonesi, and I. Meglinski, *Laser Phys. Lett.* **5**, 236 (2008).
22. J. Lademann, A. Patzelt, M. Darvin, et al., *Laser Phys. Lett.* **5**, 335 (2008).
23. R. Huber, M. Wojtkowski, J. G. Fujimoto, et al., *Opt. Express* **13**, 10523 (2005).
24. Y. Verma, K. Divakar Rao, S. K. Mohanty, and P. K. Gupta, *Laser Phys. Lett.* **4**, 686 (2007).
25. B. J. Vakoc, S. H. Yun, J. F. de Boer, et al., *Opt. Express* **13**, 5483 (2005).